Research Article

Antibiotic-loaded lactoferrin nanoparticles as a platform for enhanced infection therapy through targeted elimination of intracellular bacteria

Wei Wang[a,1], *Wanying Mo*[a,1], *Xue Xiao*[b,1], *Manying Cai*[a], *Songfu Feng*[b], *Yupeng Wang*[a,b,*], *Dongfang Zhou*[a,b,c,*]

[a] *NMPA Key Laboratory for Research and Evaluation of Drug Metabolism & Guangdong Provincial Key Laboratory of New Drug Screening & Guangdong-Hongkong-Macao Joint Laboratory for New Drug Screening, School of Pharmaceutical Sciences, Southern Medical University, Guangzhou 510515, China*
[b] *Department of Ophthalmology & Department of Ultrasonic Diagnosis, Zhujiang Hospital, Southern Medical University, Guangzhou 510515, China*
[c] *Key Laboratory of Mental Health of the Ministry of Education, Southern Medical University, Guangzhou 510515, China*

ARTICLE INFO

ABSTRACT

Intracellular bacteria can multiply inside host cells and manipulate their biology, and the efficacy of traditional antibiotic drug therapy for intracellular bacteria is limited by inadequate drug accumulation. Fighting against these stealthy bacteria has been a long-standing challenge. Here, a system of stimuli-responsive lactoferrin (Lf) nanoparticles is prepared using protein self-assembly technology to deliver broad-spectrum antibiotic rifampicin (Rif) (Rif@Lf NPs) for enhanced infection therapy through targeted elimination of intracellular bacteria. Compared to Rif@BSA NPs, the Rif@Lf NPs can specifically target macrophages infected by bacteria, thus increasing the accumulation of Rif within macrophages. Subsequently, Rif@Lf NPs with positive surface charge further displayed targeted adherence to the bacteria within macrophages and released Rif rapidly in a redox-responsive manner. Combined with the antibacterial activities of Lf and Rif, the Rif@Lf NPs showed broad-spectrum antibiotic abilities to intracellular bacteria and biofilms. As a result, the Rif@Lf NPs with high safety exhibited excellent therapeutic efficacy in the disease models of subcutaneous infection, sepsis, and bacterial keratitis. Taken together, the antibiotic-loaded Lf nanoparticles present a promising platform to combat pathogen infections through targeted elimination of intracellular bacteria.

* Corresponding authors.
  E-mail addresses: wangyupeng5@i.smu.edu.cn (Y. Wang), dfzhou@smu.edu.cn (D. Zhou).
[1] These authors contributed equally to this manuscript.

1. Introduction

Bacterial infections can lead to ulceration, sepsis, meningitis, pneumonia, and other diseases, posing a serious threat to human health [1,2]. Most bacteria are engulfed and eliminated by macrophages following infection, but a fraction of them can survive within these macrophages, known as intracellular bacteria [3-5]. These intracellular bacteria can not only evade attack from antibiotics and the host's defense system but can also hijack the infected host macrophages as Trojan horses and spread the infection through the bloodstream [6,7]. It has been reported that the major reason for the failure of clinical antibiotic therapy to eradicate intracellular bacteria is primarily due to poor membrane penetration, limited intracellular accumulation, and short retention time in macrophages of antibiotics [8,9]. Therefore, effectively addressing intracellular bacterial infections represents a pivotal and formidable challenge in the realm of clinical infection treatment.

Efficiently targeted delivery of antibiotic to infected macrophages represents a viable approach for achieving potent bactericidal effects [10–12]. Therefore, nanoparticle drug delivery systems functionalized with macrophage-targeting ligands, such as mannose, lactose, and peptide, are demonstrating increasing potential in the treatment of intracellular bacterial infection [13–16]. However, the complex preparation process of these delivery systems and the low targeting specificity to infected macrophages make them difficult for clinical applications [17,18]. Recently, protein-based drug delivery systems, such as albumin, hemoglobin, and transferrin nanoparticles, have been developed and applied for the treatment of cancers, inflammation, and bacterial infections [19–24]. Lactoferrin (Lf) is an iron-binding glycoprotein widely found in various secretory fluids, which can specifically bind to the highly expressed low-density lipoprotein receptor (LRP-1) on activated macrophage membrane, thus realizing efficient macrophage targeting [25–28]. In addition, Lf has a broad-spectrum ability to resist Gram-positive bacteria, Gram-negative bacteria, and fungi. Studies have demonstrated that Lf inhibits bacterial growth by competitively depriving bacteria of the iron required for growth [29,30]. Meanwhile, the N-terminal of Lf has a sequence that encodes lactoferricin with a positive charge, which is an antimicrobial peptide to adhere bacteria [31,32]. The above properties make Lf an ideal carrier for the delivery of antibiotics for intracellular bacterial treatment. However, there is still a gap in the current research on utilizing Lf as a delivery platform for intracellular bacterial targeting and elimination.

In this study, we prepared a system of stimuli-responsive Lf nanoparticles (Lf NPs) using protein self-assembly technology to deliver the broad-spectrum antibiotic rifampicin (Rif) (Rif@Lf NPs) for enhanced infection therapy through targeted elimination of intracellular bacteria. The Rif@Lf NPs show specific targeting of bacteria-infected macrophages, thus increasing the accumulation of Rif within macrophages. Subsequently, due to the positive surface charge, Rif@Lf NPs further exhibit targeted adherence to bacteria within macrophages, and Rif would be rapidly released from Rif@Lf NPs in a redox-responsive manner. Combining the antibacterial activities of Lf and Rif, the Rif@Lf NPs display broad-spectrum antibiotic ability to intracellular bacteria and biofilms. As a result, Rif@Lf NPs showcased excellent therapeutic efficacy in the disease models of subcutaneous infection, sepsis and bacterial keratitis (Scheme 1). Therefore, the antibiotic-loaded Lf NPs present a promising platform to combat pathogen infections through targeted elimination of intracellular bacteria.

2. Materials and methods

2.1. Materials

Vancomycin (Van), rifampicin (Rif), lactoferrin (Lf), bovine serum albumin (BSA), tris(2-carboxyethyl)phosphine (TCEP) and rhodamine B isothiocyanate (RhB) were purchased from Shanghai McLean Biochemical Technology. All chemicals were of analytical grade and did not require further purification before use. Bacterial culture and colony formatting unit (CFU) plate-related reagents, including NaCl, yeast extract, tryptone and agarose, were purchased from BD Difco Laboratories. SYTO 9/PI live/dead bacterial double stain kit was obtained from Thermo Fisher Scientific. Cell culture-related reagents, including Dulbecco's modified Eagle medium (DMEM), fetal bovine serum (FBS), penicillin, streptomycin, and phosphate-buffered saline (PBS), were purchased from Gibco Life Technologies. The TNF-a ELISA kits were purchased from Jiangsu Meimian Industrial Co., Ltd. Cell proliferation kit (CCK8) was acquired from Beyotime Biotechnology.

2.2. Preparation of Rif@Lf NPs

Lf (200 mg) was dissolved in ultrapure water (5 ml, 40 mg/ml) and centrifuged at 11,000 r/min for 10 min to remove undissolved Lf. TCEP (31.2 mg; 50 molar excess of Lf) was added and stirred at 400 rpm for 60 min and dialyzed for 12 h to remove excess TCEP. After dialysis, ethanol (1 equal volume) containing 10 mg Rif was added into the dialyzed Lf solution and stirred at 400 rpm for 30 min to prepare Rif@Lf NPs. Then, the Rif@Lf NPs solution was dialyzed for 24 h to remove the unloaded Rif. The prepared Rif@Lf NPs could be lyophilized and stored at -20 °C. Rif@BSA NPs were prepared in the same way.

2.3. Stability and release behaviors of Rif@Lf NPs

For evaluating the stability of Rif@Lf NPs, the lyophilized Rif@Lf NPs were resuspended in PBS 7.4 (containing 10 % FBS) and incubated under 37 °C. Samples were collected at 0, 6, 12, 24 and 48 h, and particle size was measured. In addition, the lyophilized Rif@Lf NPs were resuspended in PBS (pH 7.4) and incubated under 4 °C. Samples were collected at 1, 2, 3, 4, 5, 6 and 7 d, and particle size was measured. To evaluate the Rif release from Rif@Lf NPs, the lyophilized Rif@Lf NPs were resuspended in PBS (pH 7.4) with or without 1 mmol/l GSH, or with or without 1 mmol/l H_2O_2 and incubated under 37 °C with constant shaking (800 r/min). The external buffer solution (0.5 ml) was taken out at different time intervals and fresh
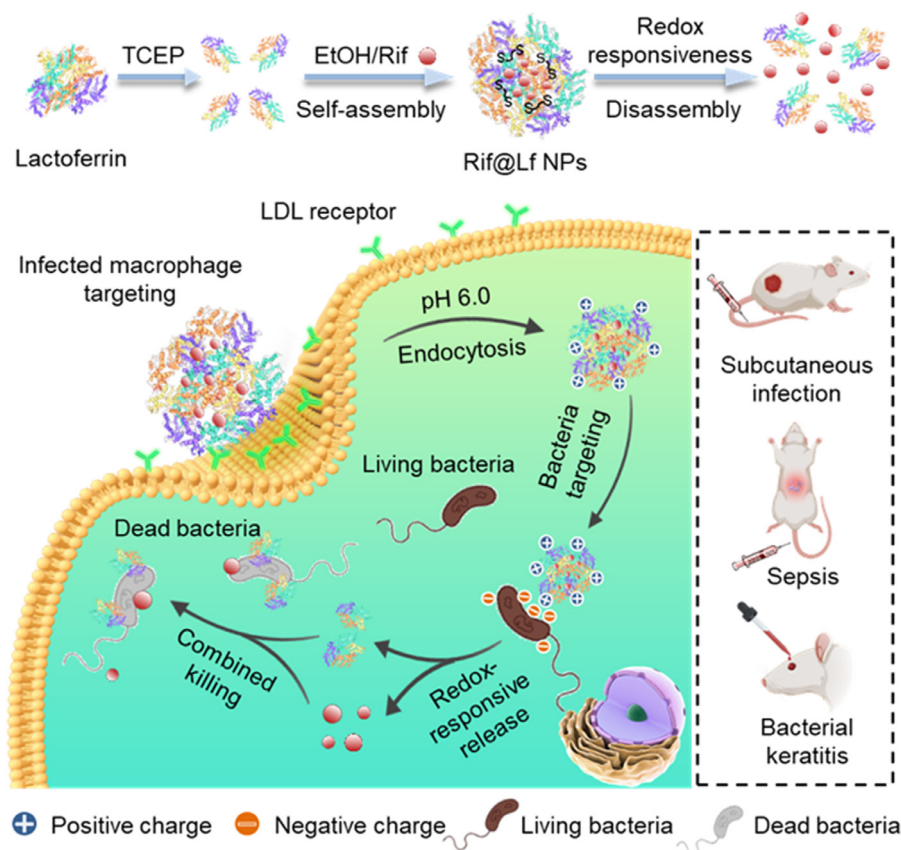
Scheme 1 – Schematic diagram of antibiotic rifampicin-loaded lactoferrin nanoparticles (Rif@Lf NPs) as a platform for enhanced infection therapy through targeted elimination of intracellular bacteria.

medium (0.5 ml) was added. The release of Rif was measured by UV–Vis.

2.4. Bactericidal effect in vitro

Escherichia coli (*E. coli*) and methicillin-resistant *Staphylococcus aureus* (MRSA) were inoculated on trypticase soy agar medium (TSA) and SOC agar plates, respectively, and incubated at 37 °C overnight, single colonies were picked and inoculated in trypticase soy broth medium (TSB) and SOC liquid medium and incubated at 37 °C for 16 h [33]. The medium was diluted to 1.0×10^5 CFU/ml and set aside. *Mycobacterium marinum* (MM) was cultured in Middlebrook 7H9 medium (with 10% albumin glucose catalase added) (BD, USA) to logarithmic phase [34]. This was then gently stirred with a grinding rod to break down bacterial aggregates, diluted with PBS, and allowed to stand for 15 min. Then, the supernatant was collected and adjusted to an OD_{600} of 0.5 (~10^8 individual bacteria/ml). The free Rif, Rif@BSA NPs, or Rif@Lf NPs were dissolved and diluted with sterile water to make the final concentration of Rif 80 µg/ml for *E. coli* and MRSA, and 5 µg/ml for MM. In the first column of the 96-well cell culture plate, the bacterial solution (180 µl) was added, and then the previously prepared free Rif solution, Rif@BSA NPs solution, Rif@Lf NPs solution, and Rif@Lf NPs solution (all 20 µl) were added respectively. After 24 h, the liquid was taken from the

bacteria, applied to lysogeny broth (LB) solid medium (*E. coli* and MRSA) or Middlebrook 7H10 agar (MM), and the plates were kept at 37 °C. After 1–2 d (*E. coli* and MRSA) or 21–30 d (MM) of incubation, plates were observed and counted for the visible colonies. Each experiment was repeated three times.

2.5. Biofilm assay

MRSA was cultured to logarithmic growth phase ($OD_{600} = 1$). Then, MRSA was resuspended and diluted to 1.0×10^5 CFU/ml with TSB, inoculated into 12-well plates, and incubated at 37 °C for 48 h. When MRSA biofilm was formed, the old medium was aspirated and discarded. Free Rif, Rif@BSA NPs and Rif@Lf NPs were dissolved with TSB at 0.32 µg/ml, added to wells, and incubated for 24 h. Then, the old medium discarded and weakly adherent planktonic bacteria were removed from the 12-well plates by washing them thrice with PBS. The adherent biofilm was immobilized by adding methanol for 15 min, removed, air-dried and stained with 0.1% (w/v) crystalline violet for 15 min. Excess dye was removed by washing with PBS three times. Crystalline violet was dissolved from the stained biofilm by adding 30% acetic acid, and its absorbance was measured at 595 nm to quantify the biofilm. Each experiment was repeated three times.

2.6. Intracellular bacteria targeting of Rif@Lf NPs

RAW264.7 cells were treated with LPS to induce them into the M1 phenotype. The cells were infected with GFP-E. coli for 3 h. The intracellular bacterial model was made, and the cells were treated with Rif_{RhB} (5 ng/ml) and nanoparticles in the following groups (control, Rif_{RhB}, Rif_{RhB}@BSA NPs and Rif_{RhB}@Lf NPs) for 24 h. DAPI was excited in the 405 nm channel with blue light, RhB was excited in the 555 nm channel with red light to represent material localization, and GFP was excited in the 488 nm channel with green light to represent bacterial localization. The targeting of lactoferrin nanomedicine to intracellular bacteria was investigated by observing the fluorescence localization of the above groups.

2.7. Killing effect of Rif@Lf NPs on intracellular bacteria

RAW264.7 cells were seeded at a density of 1×10^6 into 12 well plates for 12 h. Then, the cells were infected with E. coli, MM, and MRSA using a multiplicity of infection (MOI) of 4 for 6 h. After washing with PBS to clean the bacteria outside the cells, equal volumes of Rif, Rif@BSA NPs, or Rif@Lf NPs containing 2 fold MIC of Rif (50 µg/ml for E. coli, 1.25 µg/ml for MM, 32 µg/ml for MRSA) were added to the DMEM medium and incubated for 24 h. Subsequently, 0.1 % Triton X-100 was used to lyse the cells for 15 min. The cell lysis was plated on LB solid plates (for E. coli and MRSA) or Middlebrook 7H10 agar (for MM) after dilution with PBS, and the CFU on plates was counted after 1–2 d (for E. coli and MRSA) or 21–30 d (for MM) in a 37 °C incubator.

2.8. Pharmacokinetics profile of the Rif_{RhB}@Lf NPs

Balb/c mice (female, 4-5 weeks, 18 ± 2 g, $n = 3$) were intravenously (i.v.) injected with 0.1 ml Free Rif_{RhB}, Rif_{RhB}@BSA NPs and Rif_{RhB}@Lf NPs solution at an identical RhB dose of 2.91 mg/kg (equal to 5 mg/kg of Rif). Blood samples were collected at 5 min, 15 min, 30 min, 1 h, 3 h, 6 h and 24 h postinjection. Plasma samples were harvested by centrifugation at $1500 \times g$ for 10 min. The blood concentration of RhB was quantitatively examined using a fluorospectrophotometer.

2.9. Establishment and treatment of subcutaneous infection mouse model

The MRSA-induced abscess model was established by subcutaneous inoculation of MRSA (1×10^8 CFU/ml, 100 µl) on the backs of the mice, and the infected mice were randomly divided into four groups ($n = 5$). 2 d later (Day 0), saline, free Van, free Rif, Rif@BSA NPs, or Rif@Lf NPs were injected intravenously with a single dose of 5 mg Van/kg or 5 mg Rif/kg. The size of the wounds was observed and recorded daily. 10 d later, the mice were killed, and the infected tissues were removed from the wounds. The wound-infected tissue was ground with a tissue grinder, filtered, serially diluted, and spread on the LB solid medium. The subcutaneous tissues of the wounds were taken and fixed with 4 % paraformaldehyde, then paraffin-embedded. The paraffin blocks were sectioned and subsequently stained with H&E and Masson stains.

2.10. Establishment and treatment of an abdominal infection sepsis model in mice

Each mouse was injected subcutaneously with cyclophosphamide (150 mg/kg). 11 h later, the mice were inoculated with MRSA (saline, 1×10^8 CFU/ml, 0.1 ml bacterial suspension/injection) by intraperitoneal injection. The infected mice were randomly divided into 4 groups ($n = 8$). After 1-h infection, saline, Rif, Rif@BSA NPs, or Rif@Lf NPs were injected intravenously with a single dose of 5 mg Rif/kg. After inoculating for 24 h, three mice of each group were killed, and the blood and organs (lung, kidney, liver, spleen) were collected. The organs and tissues were ground with a tissue grinder, and the filtrate was filtered, serially diluted, and spread on the LB solid medium. The remaining mice were measured for mortality within 120 h.

2.11. Establishment and treatment of bacterial keratitis model in mice

First, mice were selected and initially screened to exclude mice with existing ocular surface diseases. Second, anesthesia was performed by intraperitoneal injection of pentobarbital (50 mg/kg), and the labeled cornea was scraped to the superficial stromal layer with a scalpel. Immediately, the MRSA (saline, 1×10^8 CFU/ml, 0.1 ml bacterial suspension/injection) was instilled into the right eye of the rat for infection. The infected mice were randomly divided into 5 groups ($n = 5$). After 2 d of infection (Day 0), saline, Rif, Rif@BSA NPs, or Rif@Lf NPs were instilled into the right eye with multiple dosing of 5 mg Rif/kg (5 µl) every day. To explore the efficacy, the mice in each group were evaluated by slit-lamp biomicroscope on Day 0, 1, 3, 5, 7 and 10 after infection treatment, respectively. The degree of repair of the infected eye was measured according to clinical features of MRSA keratitis. Each feature was graded from 0 to 4 based on three criteria: corneal opacity area, opacity density and surface regularity. 10 d later, the eyeballs were collected and ground with a tissue grinder, and the filtrate was filtered, serially diluted, and spread on the LB solid medium. The eyeball tissues of the wounds were taken and fixed with eye fixative of FAS, then paraffin-embedded. The paraffin blocks were sectioned and subsequently stained with H&E and immunofluorescent staining.

3. Results and discussion

3.1. Preparation and characterization of Rif@Lf NPs

Initially, the disulfide cross-linked Lf nanoparticles (Lf-NPs) capable of retaining drugs in the blood circulation and releasing them in an intracellular redox environment were prepared using a desolvation method [35,36]. In brief, Lf was subjected to TCEP to partially cleave its intramolecular disulfide bonds. Subsequently, the intermolecular disulfide bonds were formed between the cleaved Lf molecules via desolvation with an ethanol solution containing Rif, yielding uniformly sized Rif@Lf NPs. As shown in Fig. 1A, the measured particle diameter of the Rif@Lf NPs was 123.6 nm, with a
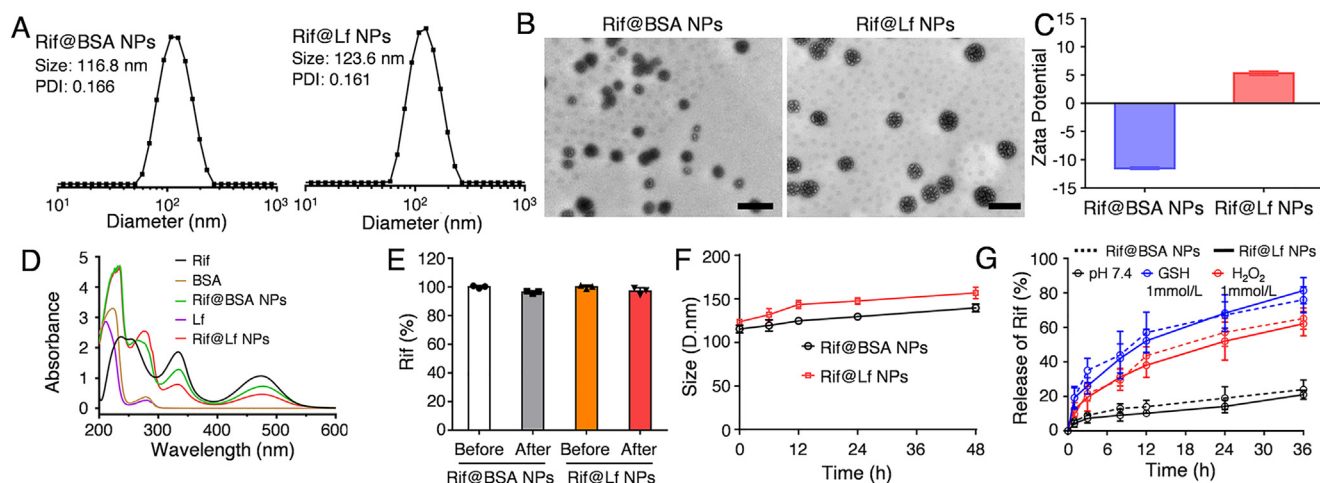
Fig. 1 – Characterization of the Rif@Lf NPs. (A) Particle size distribution of Rif@BSA NPs and Rif@Lf NPs by DLS. (B) TEM images of Rif@BSA NPs and Rif@Lf NPs. Scale bar: 200 nm. (C) Surface Zeta potential of Rif@BSA NPs and Rif@Lf NPs. (D) UV–vis spectra of free Rif, BSA NPs, Lf NPs, Rif@BSA NPs, and Rif@Lf NPs. (E) The content of Rif in Rif@BSA NPs and Rif@Lf NPs before and after lyophilization. (F) The hydrodynamic particle size of Rif@BSA NPs and Rif@Lf NPs in serum after incubation at 37 °C for 48 h. (G) Rif release profiles of Rif@BSA NPs and Rif@Lf NPs in PBS (pH 7.4) with or without GSH (1 mmol/l) or H_2O_2 (1 mmol/l). Data are represented as mean ± SD ($n = 3$).

polydispersity index (PDI) of 0.161. Transmission electron microscopy (TEM) observation demonstrated the spherical morphology of Rif@Lf NPs (Fig. 1B). The encapsulation efficiency and content of Rif in Rif@Lf NPs were 28.9 % and 2.45 %, respectively. The zeta potential of Rif@Lf NPs was +5.3 mV in PBS 7.4 (Fig. 1C). Concurrently, the disulfide cross-linked bovine serum albumin nanoparticles loading Rif (Rif@BSA NPs) were also prepared as a control to ascertain the functionality of Rif@Lf NPs. Rif@BSA NPs exhibited similar particle size and PDI (116.8 nm and 0.166) (Fig. 1A and 1B), with a zeta potential of −11.5 mV in PBS 7.4 (Fig. 1C). The characteristic UV–Vis absorption peak of Rif at 474 nm was found in both Rif@BSA NPs and Rif@Lf NPs as compared with BSA NPs and Lf NPs alone, further confirming the successful encapsulation of Rif in the protein nanoparticles (Fig. 1D).

The circular dichroism (CD) spectroscopy revealed that Rif@Lf NPs maintained the distinctive Lf-specific spectrum in the far UV region, albeit with a slight reduction in intensity, indicating the stability of the secondary structure of Lf in Rif@Lf NPs (Fig. S1). Meanwhile, the Rif content of Rif@Lf NPs and Rif@BSA NPs hardly decreased after lyophilization (Fig. 1E). Besides, Rif@Lf NPs demonstrated remarkable stability at 4 °C and 37 °C for 7 d and 48 h respectively, indicating their high stability for storage (Fig. 1F) and blood circulation (Fig. S2). Accurate drug release at the infection site is crucial for ensuring the safety and efficacy of antibiotic therapy. During the process of combating intracellular bacteria, macrophages generate oxidative stress to eliminate invading bacteria, leading to a significant increase in the levels of ROS and GSH [37]. Hence, we also investigated whether the disulfide cross-linked Rif@Lf NPs facilitated the on-demand release of Rif under intracellular redox conditions. As shown in Fig. 1G, about 28.0 % of Rif was released from the Rif@BSA NPs and Rif@Lf NPs in the simulated blood circulation condition (pH 7.4, 37 °C) within 36 h. However, the release of Rif was dramatically accelerated after incubation with 1 mmol/l GSH, or 1 mmol/l H_2O_2, with more than 60 % of released Rif, indicating that Rif@Lf NPs can responsively release Rif under intracellular redox condition of the infected macrophages.

3.2.   In vitro antibacterial effect of Rif@Lf NPs

The antibacterial activity of Rif@Lf NPs was evaluated using *E. coli*, MM, and MRSA as models of Gram-negative, mycobacterium, and drug-resistant Gram-positive bacterial strains, respectively. First, the minimum inhibitory concentration (MIC) test utilizing the resazurin method showed that the Rif@Lf NPs exhibited a MIC of 12.5 µg/ml for *E. coli*, 0.3125 µg/ml for MM, and 8.0 µg/ml for MRSA, representing a twofold decrease than that of free Rif and Rif@BSA NPs (Fig. S3). Then, the survival rate of bacteria was determined by CFU to assess the bactericidal effect of Rif@Lf NPs. For *E. coli* (Figs. 2A and S4), MM (Figs. 2B and S5), and MRSA (Figs. 2C and S6), there were negligible differences in bacterial growth between the control and the BSA NPs groups. However, attributed to the antibacterial activity of Lf, the survival rates of *E. coli*, MM, and MRSA decreased after treatment of Lf NPs. In particular, Rif@Lf NPs further enhanced the killing efficiency of bacteria, in which the bacterial survival rates were lower than 1 % of those in free Rif and Rif@BSA NPs groups (Fig. 2C and 2F). These results indicated that Rif@Lf NPs, which possess the antibacterial activities of both Lf and Rif, can efficiently and synergistically kill bacteria.

Pathogenic bacteria are capable of inducing localized purulent infection, sepsis, and septicemia in humans, in which hemolysin is one of the primary pathogenic factors [38]. As an external toxin of *Staphylococcus aureus*, hemolysin is
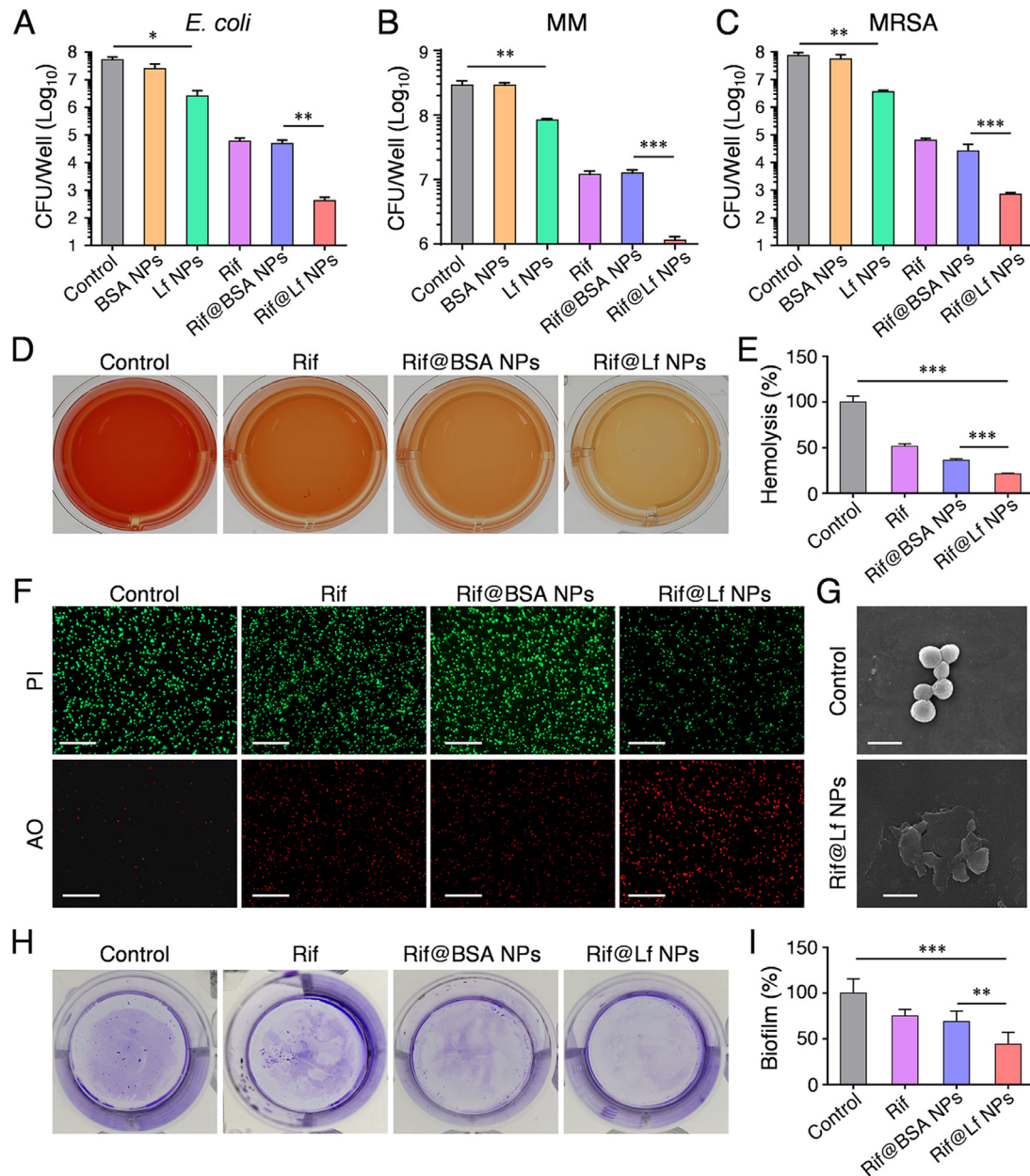
Fig. 2 – *In vitro* antibacterial effect of Rif@Lf NPs. CFU statistical results of the colonies of (A) *E.coli*, (B) MM and (C) MRSA after different treatments. (D) Photograph of hemolysin activity of MRSA after incubation with Rif, Rif@BSA NPs and Rif@Lf NPs, and (E) percentage quantitative hemolysin activity after different treatments. (F) AO/PI staining assay of MRSA by free Rif, Rif@BSA NPs and Rif@Lf NPs (scale bar: 40 μm). (G) SEM images of MRSA after incubation with and without Rif@BSA NPs and Rif@Lf NPs (scale bar: 1 μm). (H) Digital images of biofilm formation of MRSA after incubation with free Rif, Rif@BSA NPs, and Rif@Lf NPs, and (I) percentage quantitative biofilm formation after different treatments. Data are represented as mean ± SD ($n = 3$): *$P < 0.05$, **$P < 0.01$, ***$P < 0.001$.

the most important pathogenic factor causing *Staphylococcus aureus* infection. Thus, the ability of an antimicrobial agent to inhibit the toxicity of *Staphylococcus aureus* is a crucial indicator of its antibacterial activity. Here, MRSA strains were treated with different drugs, followed by observing the capacity of bacterial hemolysin in the supernatant medium to lyse rabbit red blood cells (RBC) (Fig. 2D). The hemolysis ratio of RBC was significantly reduced after Rif@Lf NPs treatment, with a 79 % decrease compared to the control

group, while the Rif group and Rif@BSA NPs group exhibited only 49 % and 63 % decrease, respectively (Fig. 2E). These results indicated that Rif@Lf NPs could effectively eliminate MRSA, thereby inhibiting the secretion of hemolysin. The antimicrobial efficacy of Rif@Lf NPs was further explored by an AO/PI staining assay. As shown in Fig. 2F, the red fluorescence signal was notably weaker than the green fluorescence signal after treatment with free Rif or Rif@BSA NPs, revealing a substantial proportion of live bacteria remained, indicating

their moderate bactericidal effects. In contrast, a substantial increase in the proportion of dead cells displaying red fluorescence was evidenced after Rif@Lf NPs treatment, demonstrating its outstanding antibacterial effect.

Finally, to further investigate the interactions between Rif@Lf NPs and bacteria, MRSA was cultured with Rif@Lf NPs and observed through scanning electron microscopy (SEM). As depicted in Fig. 2G, in contrast to the clear and smooth boundary exhibited by the bacteria in the control group, membrane disruption and deformation were observed in the bacteria treated with Rif@Lf NPs. Given that the bacterial membrane serves as a crucial protective barrier, it can be inferred that Lf enhances the permeability of the cell membrane, ultimately leading to intracellular protein leakage and irreversible damage to the bacteria. Based on previous studies, Lf can also adhere to biofilms and disrupt the biofilm structure, thus enhancing permeability and reducing antibiotic resistance [38,39]. Then, to further evaluate the impact of Rif@Lf NPs on the formation of bacterial biofilm, MRSA was subjected to different treatments, and the attached biofilms were stained with crystal violet (CV) and quantified. As shown in Fig. 2H and 2I, the biofilm formation in the free Rif group and Rif@BSA NPs group only exhibited a modest decrease of 25 % and 32 %, respectively. As expected, Rif@Lf NPs reduced approximately 60 % of biofilm formation compared to the control. The remarkable bacterial membrane disruption and biofilm removal capabilities of Rif@Lf NPs further suggested the potential for eradicating drug-resistant bacteria.

3.3. Macrophages and intracellular bacteria targeting of Rif@Lf NPs

LRP-1 is an endocytic receptor with signal transduction activity that is notably expressed and distributed on activated macrophages [40,41]. Lf exhibits a strong affinity for LRP-1, thereby enabling the targeting of activated macrophages that engulf bacteria. Encouraged by the promising *in vitro* antimicrobial properties, the capability of Rif@Lf NPs for targeted elimination of intracellular bacteria was further investigated.

Firstly, to demonstrate the targeting ability of Rif@Lf NPs to activated macrophages, confocal laser scanning microscopy (CLSM) was employed to study the endocytosis of the NPs in macrophages. Activated macrophages were labeled with FITC-CD86 fluorophore (green), and Rif was conjugated with rhodamine B isothiocyanate to yield rifampicin-rhodamine (Rif_{RhB}, red). CLSM revealed that the LPS-stimulated RAW 264.7 macrophages exhibited a higher fluorescence intensity of Rif_{RhB} incubated with Rif_{RhB}@Lf NPs compared to that of free Rif and Rif@BSA NPs (Figs. 3A and S7). The quantitative analysis of the cellular uptake of Rif in LPS-stimulated macrophages was further investigated by flow cytometry, which is consistent with CLSM result (Fig. 3C). These results indicated that Rif@Lf NPs significantly enhanced the intracellular drug accumulation due to Lf-mediated interaction with activated macrophages.

Macrophages serve as the frontline of the immune defense against pathogens, with phagosome acidification

being a crucial step in pathogen elimination. Consequently, intracellular bacteria reside in an acidic microenvironment [42]. The isoelectric point of lactoferrin is approximately 7.9, and the zeta potential of Rif@Lf NPs was measured at +14.1 mV in PBS 6.0 (which mimics the acidic microenvironment of infectious macrophages, as shown in Fig. S8). After taken by infected macrophages, the surface zeta potential of Rif@Lf NPs would change to a higher positive charge within the acidic microenvironment, which may facilitate the adherence to intracellular bacteria. So, to further investigate the targeted affinity of Rif@Lf NPs to the bacteria within macrophages, the colocalization of the Rif and bacteria was observed by CLSM. Green fluorescent protein (GFP) gene clone strain GFP-*E. coli* was used as the model bacteria. For Rif@BSA NPs-incubated macrophages, a moderate red fluorescence signal of Rif was evenly distributed, and the overlap of red and green signals was barely observed, which indicates that the Rif cannot effectively contact and interact with the bacteria in cells. Different from the Rif@BSA NPs, strong and a good overlap of red and green signals was found in macrophages incubated with Rif@Lf NPs, demonstrating a strong affinity of Rif@Lf NPs to the intracellular bacteria (Fig. 3B and 3D). Such an affinity is from the Lf with positively charged lactoferricin, which is more likely to adhere to bacteria [43–45].

Subsequently, the effectiveness of the Rif@Lf NPs in eradicating intracellular infections was assessed in macrophages infected with *E. coli* (Fig. S9), MM (Fig. S10), or MRSA (Fig. S11). The NPs significantly enhanced the antibacterial effectiveness against intracellular bacteria compared to free Rif, likely attributed to the elevated drug concentration in the cytosol. Especially, attributed to the antibacterial activity of Lf and cascaded targeting ability of Lf to macrophages and intracellular bacteria, Rif@Lf NPs demonstrated superior bactericidal potency, and the bacterial survival rates was only about 8.1 % (*E. coli*), 5.5 % (MM), and 13.9 % (MRSA) of those in Rif@BSA NPs group (Fig. 3E–3G). Intracellular bacterial infection is a primary trigger for macrophage activation [46]. Due to the limited bactericidal effect, the free Rif and Rif@BSA NPs-treated macrophages still expressed high levels of ROS (Figs. 3H and S12) and proinflammatory TNF-α (Fig. 3I), while Rif@Lf NPs can mitigate the levels of ROS and TNF-α. These findings demonstrated the excellent capability of Rif@Lf NPs for the targeted elimination of intracellular bacteria, showing substantial potential as a platform for enhanced infection therapy *in vivo*.

3.4. In vivo therapeutic effect of Rif@Lf NPs for subcutaneous infection and sepsis

The therapeutic efficacy of Rif@Lf NPs was comprehensively assessed *in vivo*. First, the pharmacokinetics profile of the Rif@Lf NPs was examined in Balb/c mice. Free Rif_{RhB}, Rif_{RhB}@BSA NPs and Rif_{RhB}@Lf NPs were administrated intravenously (*i.v.*) at a dose of 2.91 mg RhB/kg (equal to 5 mg Rif/kg). The blood concentrations of Rif_{RhB} were then examined by using a fluorospectrophotometer. The blood clearance half-life periods ($T_{1/2}$) of Rif_{RhB} in the Rif_{RhB}@BSA NPs group and Rif_{RhB}@Lf NPs group were 4.24 h and 3.11 h,
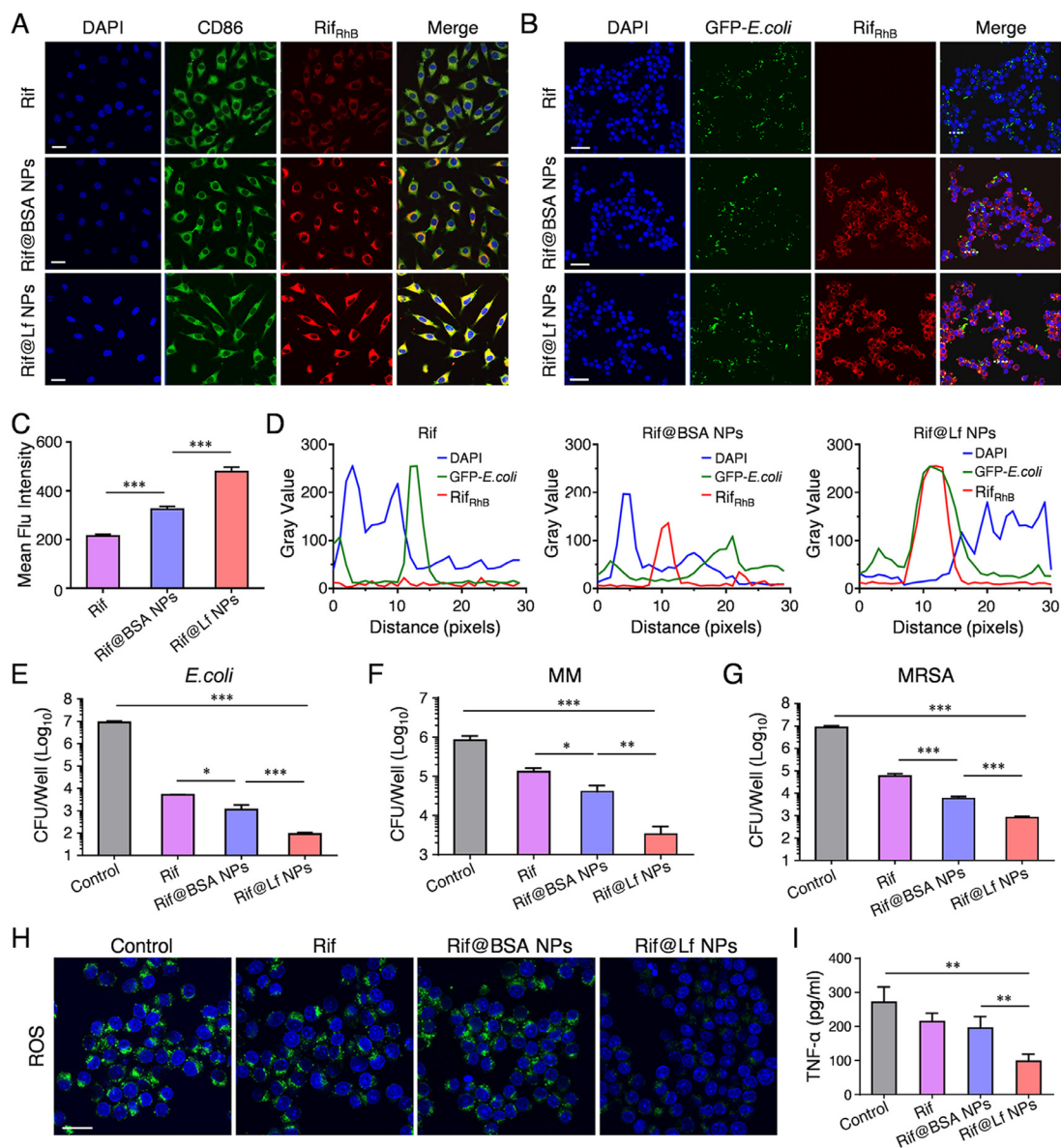
Fig. 3 – Targeted killing effect of Rif@Lf NPs for intracellular bacteria. (A) CLSM images of activated macrophages (CD86) after incubation with free Rif_{RhB}, Rif_{RhB}@BSA NPs, or Rif_{RhB}@Lf NPs for 24 h. (Scale bar: 20 µm). (B) CLSM images of intracellular bacteria (GFP-*E.coli*) after incubation with free Rif_{RhB}, Rif_{RhB}@BSA NPs or Rif_{RhB}@Lf NPs for 24 h. Colocalization analysis was performed on the cells labeled by white dashed line. (Scale bar: 40 µm). (C) Mean fluorescence intensity of Rif_{RhB} in activated macrophages. (D) Fluorescence intensity profiles across the merge images of DAPI, GFP-*E.coli*, and Rif_{RhB}. CFU statistical results of (E) *E.coli* colonies, (F) MM colonies, and (G) MRSA colonies after different treatments. (H) Fluorescent images of ROS production in MRSA-infected RAW 264.7 macrophages after different treatments. (Scale bar: 20 µm). (I) Content of TNF-α in MRSA-infected macrophages after different treatments. Data are represented as mean ± SD ($n = 3$): *$P < 0.05$, **$P < 0.01$, ***$P < 0.001$.

respectively, longer than that of the free Rif_{RhB} group ($T_{1/2} = 0.61$ h) (Fig. S13), suggesting that the formulation of Rif_{RhB} in protein nanoparticles prolonged the blood circulation. Subsequently, a subcutaneous infection mouse model was established. Mice were subcutaneously inoculated with MRSA (1×10^8 CFUs), and a single dose of saline, free Van (first-line clinical drug of MRSA, non-drug resistant) [40], free Rif (broad-spectrum antibiotic, a certain degree of drug resistance), Rif@BSA NPs, or Rif@Lf NPs (5 mg Van/kg, or 5 mg

Rif/kg) was administered intravenously after 2 d of infection (Fig. 4A). By the end of the experiment (Day 10), both free Van and free Rif groups exhibited relatively slower wound healing rates (Fig. 4B) than NPs groups, which may be attributed to the limited antibacterial efficacy of small molecular drugs against intracellular bacteria. While, the mice in NPs groups showed outstanding wound healing rates effect, especially Rif@Lf NPs group showed nearly healed wounds (Fig. 4B). The quantitative assessment of the relative wound area also
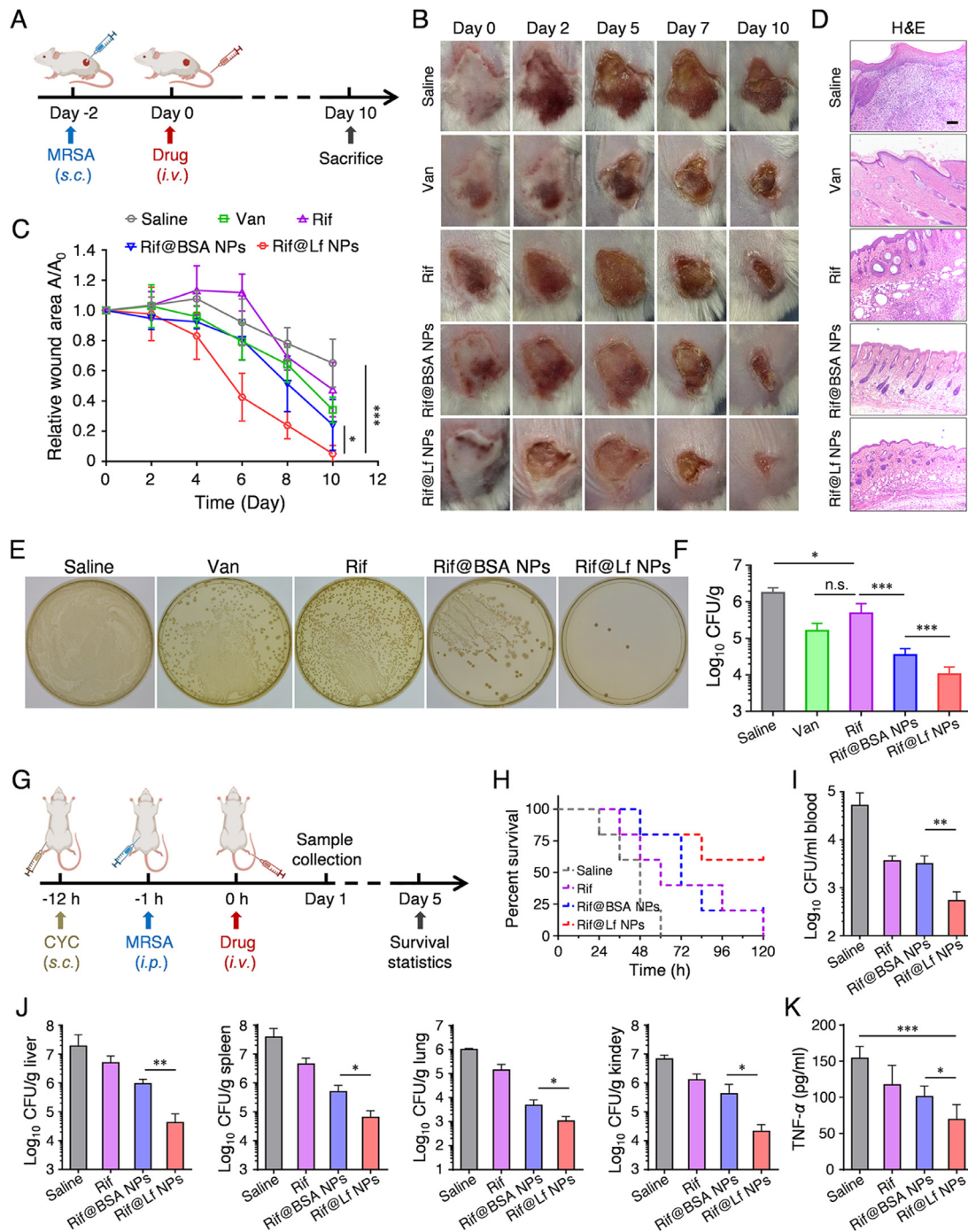
Fig. 4 – *In vivo* therapeutic effect of Rif@Lf NPs for subcutaneous infection and sepsis. (A) Schematic of the treatment design of subcutaneous infection. (B) Photographic images of the infected wound healing in treated mice. (C) Relative area of subcutaneous infected wound in treated mice. (D) Histological analysis of infected skin in treated mice by H&E staining on Day 10. Scale bar: 200 mm. (E) Photographs of bacterial colonies obtained from infected tissues of mice after treatment with Van, Rif, Rif@BSA NPs, or Rif@Lf NPs. (F) Quantitative statistics of the number of bacterial colonies through standard plate counting assay. Data are represented as the mean ± SD ($n = 5$). (G) Schematic of the experimental design of sepsis treatment. (H) Survival rates of all treated mice in 120 h. Bacterial numbers in the (I) blood and (J) different organs (liver, spleen, lung, and kidney) from mice after treatment with free Rif, Rif@BSA NPs, or Rif@Lf NPs for 24 h. (K) TNF-α level in the blood from mice after treatment with free Rif, Rif@BSA NPs or Rif@Lf NPs for 24 h. Data are represented as mean ± SD ($n = 3$). *$P < 0.05$, **$P < 0.01$, ***$P < 0.001$.

provided clear evidence of the best wound healing effect after 10 d of Rif@Lf NPs treatment (Fig. 4C). H&E staining further confirmed that Rif@Lf NPs reduced inflammatory cell infiltration, fibroblast migration, and proliferation in the wounded skin, outperforming the other groups (Fig. 4D). Examination of Masson's trichrome staining images at the different stages of wound healing revealed the presence of new hair follicles and collagen deposition exclusively in the mice treated with Rif@Lf NPs, indicating a relatively more rapid wound healing process (Fig. S14). The bacterial content in the wounded skin was notably reduced after being treated with antibiotics (Fig. 4E). The bacterial quantity in the wounded skin was 1.05×10^5 CFU/g in the Rif@Lf NPs group, much lower than that of the free Van group (2.28×10^6 CFU/g), the free Rif group (4.85×10^6 CFU/g) and Rif@BSA NPs group (3.48×10^5 CFU/g) (Fig. 4F). These results demonstrated that, compared with free drugs and Rif@BSA NPs, Rif@Lf NPs could enhance the intracellular bacteria elimination *in vivo*, thus accelerating the healing of infected wounds.

The above model proved that Rif@Lf NPs exhibited a good therapeutic effect on local bacterial infection. To screen the effect of Rif@Lf NPs on systemic bacterial infection, a murine bacterial sepsis model was established by intraperitoneal injection of a lethal dose of MRSA (1×10^8 CFU) into immunocompromised mice treated with cyclophosphamide (Fig. 4G). Sepsis represents a life-threatening, systemic inflammatory response triggered by fungal or bacterial pathogens. Despite advancements in antibiotic therapy, the mortality rate associated with sepsis remains elevated, with the incapacity to eliminate intracellular bacteria standing out as a primary causative factor [47]. After 1 h of bacterial injection, the mice were divided into four groups and treated with saline, free Rif, Rif@BSA NPs, and Rif@Lf NPs *via* tail vein injection, respectively. The mouse survival rates were monitored over time. The lethal dose of MRSA led to the death of all saline-treated mice within 60 h, while the mice treated with free Rif and Rif@BSA NPs all died within 120 h (Fig. 4H). In comparison, a significant survival benefit was observed in mice treated with Rif@Lf NPs, resulting in increased survival rates for 3 out of 5 mice. Additionally, the bacterial survival in blood and key organs was examined in another cohort of mice. After being treated with different drugs for 24 h, the bacterium numbers in blood (Fig. 4I) and major organs (Fig. 4J) were obviously lower in mice treated with Rif@Lf NPs compared with those of the free Rif-treated mice and Rif@BSA NPs-treated mice (Fig. S15). The decrease in bacterial infection in blood and organs also contributed to a reduction in the levels of proinflammatory TNF-α, thereby reducing systemic inflammation in mice (Fig. 4K). All these results from both local and systemic infection therapy demonstrated that Rif@Lf NPs acted as a highly effective antimicrobial nano-platform by cascaded targeting of macrophages and intracellular bacteria to enhance the bioavailability of Lf and Rif.

3.5. *In vivo therapeutic effect of Rif@Lf NPs for bacterial keratitis*

Bacterial keratitis is one of the common corneal infection blind-causing diseases. It is characterized by the infiltration of inflammatory cells and the destruction of corneal structures

[48]. Frequently dripping of high concentrations of antibiotic eye fluid in the acute phase is the main clinical strategy for bacterial keratitis. However, topical-free antibacterial drugs show limited therapeutic effects in killing drug-resistant or intracellular bacteria [49,50]. The Rif@Lf NPs have demonstrated the targeted bactericidal effect on intracellular bacteria, and the solution exhibits excellent stability over extended periods of storage, which is highly suitable for use as an antibacterial eye drop for the treatment of bacterial keratitis.

Thus, to evaluate the effect of Rif@Lf NPs on bacterial keratitis, we established a mouse model of keratitis infected by MRSA (Day 2) (Fig. 5A). The morphology of the anterior segment following various topical ocular treatments was examined using slit lamp microscopy, and relevant clinical scores were recorded after infection. As depicted in Fig. 5B, no aqueous humor flares, anterior chamber fibrin, or cataracts were observed in healthy mice through the slit-lamp. All modeling mouse corneas displayed clinical symptoms with severe purulent ulceration and dense opacity, which almost entirely covered the cornea two d after infection, indicating the successful establishment of bacterial keratitis. Then, saline, Rif, Rif@BSA NPs, or Rif@Lf NPs were instilled into the right eye with multiple dosing of 5 mg Rif/kg (5 μl) every day. For the saline and Rif-treated groups, the corneas exhibited continuous morphological changes and purulent corneal ulcers in the corneal epithelium within 10 d after infection, resulting in severe corneal defects. Following treatment with Rif@BSA NPs and Rif@Lf NPs, the symptoms of the infected cornea gradually improved, and the corneal morphology returned to normal, particularly for Rif@Lf NPs treatment. Moreover, the clinical total score of mice after Rif@Lf NPs treatment gradually decreased and reached the normal score level on Day 10 (Fig. 5C). The host response to MRSA infection was also examined by quantifying the number of viable bacteria in corneal tissue cultured overnight on MRSA plates. Following the Rif@Lf NPs treatment, almost no colony formation was observed compared to the other treatment groups (Fig. 5D and 5E), further confirming the superior therapeutic effect of Rif@Lf NPs for bacterial keratitis.

A series of histological analyses were further conducted on mouse corneas to evaluate corneal healing. Corneal histological analysis by H&E staining revealed an intact corneal structure and clear corneal layers following the Rif@Lf NPs treatment (Fig. 5F). Enlarged images further demonstrated minimal infiltrated inflammatory cells and a significant reduction in corneal collagen fiber edema in Rif@Lf NPs treatment group. In contrast, the saline, Rif, and Rif@BSA NPs treatments exhibited abnormal corneal structure and extensive inflammatory cell infiltration in the mouse corneal stroma. To further verify the histological analysis results, immunofluorescence staining was conducted on the various groups. The ROS staining (red) indicates that Rif@Lf NPs treatment exhibited only faint red fluorescence, signifying a low presence of inflammatory cells (Fig. 5G). Meanwhile, the expression of α-smooth muscle actin (α-SMA, green) was observed to analyze myofibroblast formation and corneal scarring (Fig. 5H). Prolonged myofibroblast activity can lead to corneal scarring. The fluorescence images revealed that the α-SMA expression was not significant in Rif@Lf NPs group,
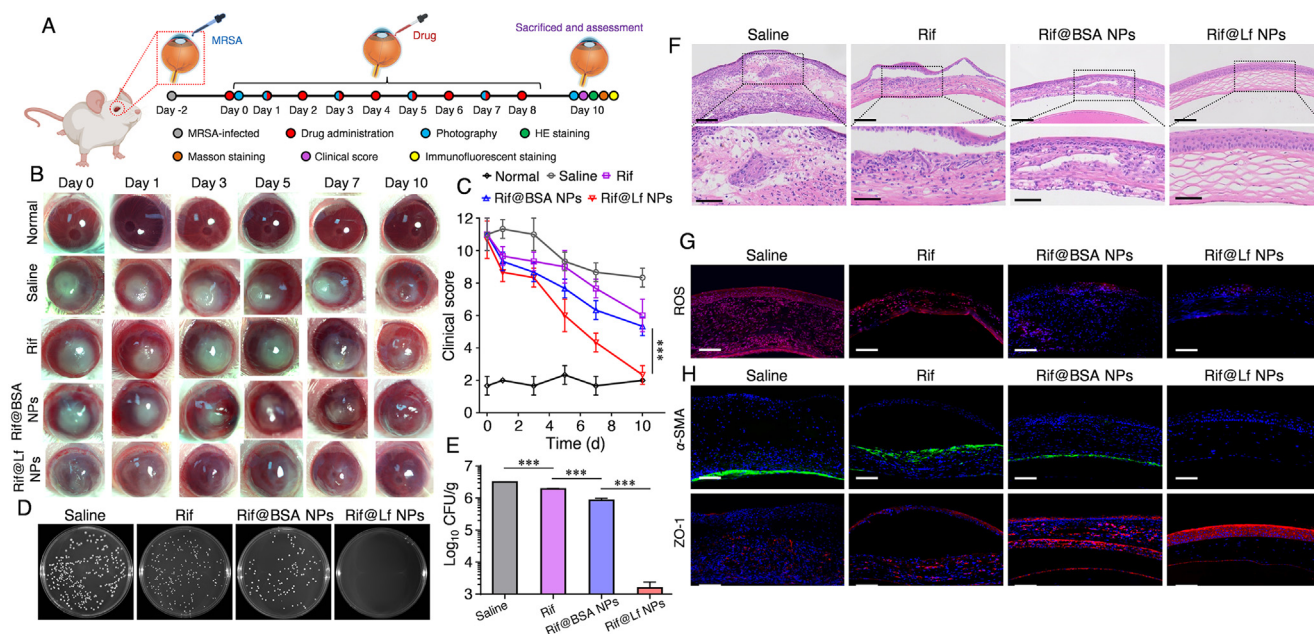
Fig. 5 – *In vivo* therapeutic effect of Rif@Lf NPs for bacterial keratitis. (A) Schematic illustration of the establishment, administration and sacrifice of the MRSA-infected keratitis model. (B) Representative slit-lamp micrograph appearance of MRSA-infected keratitis in mice after treatment with free Rif, Rif@BSA NPs or Rif@Lf NPs at a series of observation time points within the therapeutic procedure. (C) Evaluation of the corresponding clinical score (0–12) by three oculists following three criteria (opacity area, surface regularity, opacity density). (D) Photographs of bacterial colonies formed on TSB-agar plates from corneal tissues. (E) Quantitative statistics of the number of bacterial colonies through standard plate counting assay. (F) Representative histopathological observation of inflammation of H&E in mice cornea paraffin sections after treatment. Scale bar: 200 mm. (G) Immunofluorescence images for the detection of ROS production of the monolayer H&E MXenes in the cornea of mice. Scale bar: 100 μm. (H) Immunofluorescent staining of α-SMA and ZO-1 in the cornea infected with MRSA on Day 10. Scale bar = 100 μm. Data are represented as mean ± SD ($n = 5$): *P < 0.05, **P < 0.01, ***P < 0.001.

suggesting that the substantial myofibroblast activation was not induced. In contrast, in the saline, Rif, and Rif@BSA NPs groups, the fluorescence intensity of α-SMA was pronounced, indicating high myofibroblast activation, possibly linked to the significant immune response in these groups (Fig. 5H). Additionally, immunofluorescence staining and quantitative data analysis were conducted on the tight junction protein zonula occludens-1 (ZO-1, red) in the epithelial monolayer (Fig. 5H). The expression level of ZO-1 in the Rif@Lf NPs group was significantly higher than in the Rif and Rif@BSA NPs groups, indicating that it could effectively promote the regeneration of the corneal. Consequently, Rif@Lf NPs killed the bacteria and effectively alleviated the host's inflammatory response to bacterial keratitis.

Finally, to ensure the highly effective and precise treatment can be potentially translated into practical application, a series of safety studies of Rif@Lf NPs were conducted *in vivo*. The body weight of the Rif@Lf NPs-treated mice remained stable throughout the treatment period (lasting up to 10 d) (Fig. S16A). Furthermore, the Rif@Lf NPs-based treatment showed no potential impact on the blood biochemical parameters, including alanine aminotransferase (ALT), aspartate aminotransferase (AST), albumin (ALB), UREA, and creatinine (CR) (Fig. S16B), indicating the good hemocompatibility. Taken together, the excellent therapeutic effect and safety of Rif@Lf NPs ensure the potential clinical transformation prospect.

4.   Conclusion

In summary, we prepared a system of stimuli-responsive Lf nanoparticles using protein self-assembly technology to deliver a broad-spectrum antibiotic Rif (Rif@Lf NPs) for enhanced infection therapy through targeted elimination of intracellular bacteria. Our studies have shown that, compared with free Rif and Rif@BSA NPs, Rif@Lf NPs can specifically bind to the LRP-1 on macrophages infected by bacteria, thus increasing the accumulation of Rif within macrophages. Subsequently, due to the positive surface charge, the Rif@Lf NPs further displayed targeted adherence to bacteria within macrophages. Under the redox intracellular environment, Rif@Lf NPs exhibited responsive disassembly to release Rif. Thus, combining the antibacterial activity of Lf with Rif, the Rif@Lf NPs showed broad-spectrum antibiotic abilities to intracellular bacteria *in vitro* and *in vivo*. Compared with free Rif and Rif@BSA NPs, Rif@Lf NPs demonstrated excellent therapeutic effects in a series of disease models, including accelerating the healing of infected wounds in a subcutaneous infection model, decreasing systemic

inflammation and mortality of mice in a sepsis model, and promoting the regeneration of the corneal in a bacterial keratitis model. Furthermore, Rif@Lf NPs showed high safety to mice. Overall, this study provides a promising antibiotic-loaded Lf nanoparticles platform to combat pathogen infections through the targeted elimination of intracellular bacteria.

Conflicts of interest

The authors report no conflicts of interest. The authors alone are responsible for the content and writing of this article.

Acknowledgments

Supplementary materials

Supplementary material associated with this article can be found, in the online version, at doi:10.1016/j.ajps.2024.100926.

REFERENCES

[1] GBD 2019 Antimicrobial Resistance CollaboratorsGlobal mortality associated with 33 bacterial pathogens in 2019: a systematic analysis for the Global Burden of Disease Study 2019. Lancet 2022;400(10369):2221–48.

[2] Willyard C. The drug-resistant bacteria that pose the greatest health threats. Nature 2017;543(7643):15.

[3] Thi EP, Lambertz U, Reiner NE. Sleeping with the enemy: how intracellular pathogens cope with a macrophage lifestyle. PLoS Pathog 2012;8(3):e1002551.

[4] Kamaruzzaman NF, Kendall S, Good L. Targeting the hard to reach: challenges and novel strategies in the treatment of intracellular bacterial infections. Br J Pharmacol 2017;174(14):2225–36.

[5] Flannagan RS, Cosío G, Grinstein S. Antimicrobial mechanisms of phagocytes and bacterial evasion strategies. Nat Rev Microbiol 2009;7(5):355–66.

[6] Finlay BB, McFadden G. Anti-immunology: evasion of the host immune system by bacterial and viral pathogens. Cell 2006;124(4):767–82.

[7] Plüddemann A, Mukhopadhyay S, Gordon S. Innate immunity to intracellular pathogens: macrophage receptors and responses to microbial entry. Immunol Rev 2011;240(1):11–24.

[8] Abed N, Couvreur P. Nanocarriers for antibiotics: a promising solution to treat intracellular bacterial infections. Int J Antimicrob Agents 2014;43(6):485–96.

[9] Radovic-Moreno AF, Lu TK, Puscasu VA, Yoon CJ, Langer R, Farokhzad OC. Surface charge-switching polymeric nanoparticles for bacterial cell wall-targeted delivery of antibiotics. ACS Nano 2012;6(5):4279–87.

[10] Makabenta JMV, Nabawy A, Li CH, Schmidt-Malan S, Patel R, Rotello VM. Nanomaterial-based therapeutics for antibiotic-resistant bacterial infections. Nat Rev Microbiol 2021;19(1):23–36.

[11] Briones E, Colino CI, Lanao JM. Delivery systems to increase the selectivity of antibiotics in phagocytic cells. J Control Release 2008;125(3):210–27.

[12] Chen X, Zou Y, Zhang S, Fang P, Li S, Li P, et al. Multi-functional vesicles improve Helicobacter pylori eradication by a comprehensive strategy based on complex pathological microenvironment. Acta Pharm Sin B 2022;12(9):3498–512.

[13] Gao C, Kwong CHT, Tang M, Liu J, Kam H, Li S, et al. A bacterially engineered macrophage sponge as a neutralization decoy to treat bacterial infection. Matter 2023;6:1–2.

[14] Yoo J, Park C, Yi G, Lee D, Koo H. Active targeting strategies using biological ligands for nanoparticle drug delivery systems. Cancers 2019;11(5):640.

[15] Shao Q, Ding T, Pan F, Li G, Shen S, Qian J, et al. Protein corona mediated liposomal drug delivery for bacterial infection management. Asian J Pharm Sci 2022;17(6):855–66.

[16] Wang W, Guo H, Lin S, Xiao X, Liu Y, Wang Y, et al. Biosafety materials for tuberculosis treatment. Biosafety Health 2022;4(4):258–68.

[17] Elhassan E, Devnarain N, Mohammed M, Govender T, Omolo CA. Engineering hybrid nanosystems for efficient and targeted delivery against bacterial infections. J Control Release 2022;351:598–622.

[18] Xiong MH, Li YJ, Bao Y, Yang XZ, Hu B, Wang J. Bacteria-responsive multifunctional nanogel for targeted antibiotic delivery. Adv Mater 2012;24(46):6175–80.

[19] Salatin S, Jelvehgari M, Maleki-Dizaj S, Adibkia K. A sight on protein-based nanoparticles as drug/gene delivery systems. Ther Deliv 2015;6(8):1017–29.

[20] Martínez-López AL, Pangua C, Reboredo C, Campión R, Morales-Gracia J, Irache JM. Protein-based nanoparticles for drug delivery purposes. Int J Pharm 2020;581:119289.

[21] Li S, Sun W, Ouyang M, Yu B, Chen Y, Wang Y, et al. Hemoglobin-related biomaterials and their applications. Adv Nanobiomed Res 2023;3(3):2200103.

[22] He Y, Fang Y, Zhang M, Zhao Y, Tu B, Shi M, et al. Remodeling "cold" tumor immune microenvironment via epigenetic-based therapy using targeted liposomes with in situ formed albumin corona. Acta Pharm Sin B 2022;12(4):2057–73.

[23] Wang Y, Yu J, Luo Z, Shi Q, Liu G, Wu F, et al. Engineering endogenous tumor-associated macrophage-targeted biomimetic nano-RBC to reprogram tumor immunosuppressive microenvironment for enhanced chemo-immunotherapy. Adv Mater 2021;33(39):2103497.

[24] Peng Y, Chen L, Ye S, Kang Y, Liu J, Zeng S, et al. Research and development of drug delivery systems based on drug transporter and nano-formulation. Asian J Pharm Sci 2020;15(2):220–36.

[25] Sienkiewicz M, Jaśkiewicz A, Tarasiuk A, Fichna J. Lactoferrin: an overview of its main functions, immunomodulatory and antimicrobial role, and clinical significance. Crit Rev Food Sci Nutr 2022;62(22):6016–33.

[26] Luo S, Yang Y, Zhao T, Zhang R, Fang C, Li Y, Zhang Z, Gong T. Albumin-based silibinin nanocrystals targeting activated hepatic stellate cells for liver fibrosis therapy. ACS Appl Mater 2023;15(6):7747–58.

[27] Vash B, Phung N, Zein S, DeCamp D. Three complement-type repeats of the low-density lipoprotein receptor-related protein define a common binding site for RAP, PAI-1, and lactoferrin. Blood 1998;92(9):3277–85.

[28] Zhao Y, Yang Y, Zhang J, Wang R, Cheng B, Kalambhe D. Lactoferrin-mediated macrophage targeting delivery and patchouli alcohol-based therapeutic strategy for inflammatory bowel diseases. Acta Pharm Sin B 2020;10(10):1966–76.

[29] Rosa L, Cutone A, Lepanto MS, Paesano R, Valenti P. Lactoferrin: a natural glycoprotein involved in iron and inflammatory homeostasis. Int J Mol Sci 2017;18(9):1985.

[30] Arnold RR, Cole MF, McGhee JR. A bactericidal effect for human lactoferrin. Science 1977;197(4300):263–5.

[31] Arranz-Trullén J, Lu L, Pulido D, Bhakta S, Boix E. Host antimicrobial peptides: the promise of new treatment strategies against tuberculosis. Front Immunol 2017;8:1499.

[32] Andersen JH, Jenssen H, Sandvik K, Gutteberg TJ. Anti-HSV activity of lactoferrin and lactoferricin is dependent on the presence of heparan sulphate at the cell surface. J Med Virol 2004;74(2):62–71.

[33] Wang W, Hu Z, Mo W, Ouyang M, Lin S, Li X, et al. Ultrastable *in-situ* silver nanoparticle dressing for effective prevention and treatment of wound infection in emergency. Eng Regenerat 2024;5(1):111–23.

[34] Li B, Wang W, Zhao L, Wu Y, Li X, Yan D, et al. Photothermal therapy of tuberculosis using targeting pre-activated macrophage membrane-coated nanoparticles. Nat Nanotechnol 2024;8:2373.

[35] Yu Y, Chen S, Wang Y, Zhou D, Wu D. Fighting against drug-resistant tumor by the induction of excessive mitophagy with transferrin nanomedicine. Macromol Biosci 2024;24(2):e2300116.

[36] Yasuda K, Maeda H, Kinoshita R, Minayoshi Y, Mizuta Y, Nakamura Y, et al. Encapsulation of an Antioxidant in Redox-Sensitive Self-Assembled Albumin Nanoparticles for the Treatment of Hepatitis. ACS Nano 2023;7(17):16668–81.

[37] Li B, Wang W, Zhao L, Yan D, Li X, Gao Q, et al. Multifunctional AIE nanosphere-based "Nanobomb" for trimodal imaging-guided photothermal/photodynamic/ pharmacological therapy of drug-resistant Bacterial infections. ACS Nano 2023;17(5):4601–18.

[38] Stewart PS, Costerton JW. Antibiotic resistance of bacteria in biofilms. Lancet 2001;358(9276):135–8.

[39] Al-Mogbel MS, Menezes GA, Elabbasy MT, Alkhulaifi MM, Hossain A, Khan MA. Effect of synergistic action of bovine lactoferrin with antibiotics on drug resistant bacterial pathogens. Medicina 2021;57(4):343.

[40] He X, Dai L, Ye L, Sun X, Enoch O, Hu R, et al. A vehicle-free antimicrobial polymer hybrid gold nanoparticle as synergistically therapeutic platforms for *staphylococcus aureus* infected wound healing. Adv Sci 2022;9(14):e2105223.

[41] Lillis AP, Mikhailenko I, Strickland DK. Beyond endocytosis: LRP function in cell migration, proliferation and vascular permeability. J Thromb Haemost 2005;3(8):1884–93.

[42] Sedlyarov V, Eichner R, Girardi E, Essletzbichler P, Goldmann U, Nunes-Hasler P, et al. The bicarbonate transporter SLC4A7 plays a key role in macrophage phagosome acidification. Cell Host Microbe 2018;23:766–74.

[43] Gottenbos B, Grijpma DW, van der Mei HC, Feijen J, Busscher HJ. Antimicrobial effects of positively charged surfaces on adhering gram-positive and gram-negative bacteria. J Antimicrob Chemother 2001;48(1):7–13.

[44] Vogel HJ. Lactoferrin, a bird's eye view. Biochem Cell Biol 2012;90(3):233–44.

[45] Liang Y, Liang Y, Zhang H, Guo B. Antibacterial biomaterials for skin wound dressing. Asian J Pharm Sci 2022;17(3):353–84.

[46] Qiu P, Liu Y, Zhang J. The role and mechanisms of macrophage autophagy in sepsis. Inflammation 2019;42:6–19.

[47] Hou X, Zhang X, Zhao W, Zeng C, Deng B, McComb DW, Du S, Zhang C, Li W, Dong Y. Vitamin lipid nanoparticles enable adoptive macrophage transfer for the treatment of multidrug-resistant bacterial sepsis. Nat Nanotechnol 2020;15:41–6.

[48] Tuft S, Somerville TF, Li JO, Neal T, De S, Horsburgh MJ, et al. Bacterial keratitis: identifying the areas of clinical uncertainty. Prog Retin Eye Res 2022;89:101031.

[49] Ruddaraju LK, Pammi SVN, Guntuku GA, Padavalaa VS, Kolapalli VRM. A review on anti-bacterials to combat resistance: from ancient era of plants and metals to present and future perspectives of green nano technological combinations. Asian J Pharm Sci 2020;15(1):42–59.

[50] Li B, Wang W, Song W, Zhao Z, Tan Q, Zhao Z, et al. Antiviral and anti-inflammatory treatment with multifunctional alveolar macrophage-like nanoparticles in a surrogate mouse model of COVID-19. Adv Sci 2021;8(13):2003556.